Article:
Xu, S, Gao, X, Hua, Y orcid.org/0000-0002-7457-1813 et al. (3 more authors) (2020) Rapid deposition of WS2 platelet thin films as additive-free anode for sodium ion batteries with superior volumetric capacity. Energy Storage Materials, 26. pp. 534-542. ISSN 2405-8297

https://doi.org/10.1016/j.ensm.2019.11.026

Energy Storage Materials

Rapid deposition of WS2 platelets thin film as additive-free anode for sodium ion batteries with superior volumetric capacity

--Manuscript Draft--

Manuscript Number:	ENSM_2019_123R4
Article Type:	Research Paper
Section/Category:	Electrochemical energy storage
Keywords:	Fast deposition; vertically-aligned WS2 platelet; additive-free; sodium ion battery anode; high volumetric capacity.
Corresponding Author:	Shusheng Xu Institute of Functional Surfaces, School of Mechanical Engineering, University of Leeds Leeds, UNITED KINGDOM
First Author:	Shusheng Xu
Order of Authors:	Shusheng Xu
	Xiaoming Gao
	Yong Hua
	Anne Neville
	Yanan Wang
	Kan Zhang
Manuscript Region of Origin:	Europe
Abstract:	One of the key issues hampering the practical applications of powerful and thin sodium-ion batteries (SIBs) is low volumetric capacity. The purpose of this study is to report an innovative sputtering strategy to directly construct the vertically-aligned WS2 columnar platelet film with low-tortuosity pores (VA/LT-WS2) on an Al foil as an additive-free anode. Profiting from a 6 nm carbon overlayer on the top of the thickness-controllable film electrode (VA/LT-WS2/C), the vertical feature of WS2 and carbon layer enable high efficiency of ion and electron transportation pathways, respectively. The 2.8 mm VA/LT-WS2/C film anode exhibits a high volumetric capacity of 1,339 mAh·cm-3 at 100 mA·g-1, of which 30.2% is recorded when the current density gets a 50-fold increase from 100 to 5,000 mA·g-1. Its gravimetric capacity of 366.8 mAh·g-1 is comparable to the reported WS2 based anode materials for SIBs. Moreover, it is interesting to note that the discontinuous carbon layer (6 nm thickness) protects the presence of solid electrolyte interphase (SEI) layer from cracking caused by the volume expansion of WS2 anode, and less than 16.7% volumetric capacity fading is presented after 300 cycles. It outperforms most of the recently reported outstanding SIBs anode materials. The SIB full cell exhibited a reversible volumetric capacity of 554 mAh·cm-3 at 50 mA·g-1 when the additive-free anode was applied in the VA/LT-WS2/C // Na2V3(PO4)3/C full cell, demonstrating the potential of the physical sputtering VA/LT-WS2/C for further battery development.
Suggested Reviewers:	Chen Zhang, Ph.D Associate Professor, Tianjin University zhangc@tju.edu.cn Professor Zhang is an expert in the exploring novel method for fabricating battery material.
	Dae-Eun Kim, Ph.D Professor, Yonsei University kimde@yonsei.ac.kr Prof. Kim is an expert in the PVD film fabrication for multi-function application.
Opposed Reviewers:	
Response to Reviewers:	The “Response to Editor and Reviewers’ Comments” file has been attached, in which we have studied the editor and reviewers’ comments carefully and have made

	revisions. This file contains lots of graphs which can't be shown in this box. Please find all the responds to editor and reviewers in the attached.

Rapid deposition of WS_2 platelets thin film as additive-free anode for sodium ion batteries with superior volumetric capacity

Shusheng Xu [a,*], Xiaoming Gao [b], Yong Hua [a], Anne Neville [a], Yanan Wang [b,*], Kan Zhang [c]

[a] *Institute of Functional Surfaces, School of Mechanical Engineering, University of Leeds, Leeds, LS2 9JT, UK*

[b] *State Key Laboratory of Solid Lubrication, Lanzhou Institute of Chemical Physics, Chinese Academy of Sciences, Lanzhou 730000, People's Republic of China*

[c] *MIIT Key Laboratory of Advanced Display Materials and Devices, Institute of Optoelectronics and Nanomaterials, School of Materials Science and Engineering, Nanjing University of Science and Technology, Nanjing 210094, People's Republic of China*

Corresponding Authors: E-mail address (Anne Neville): a.neville@leeds.ac.uk.

E-mail address (Yanan Wang): ynwang@licp.cas.cn.

Rapid deposition of WS_2 platelets thin film as additive-free anode for sodium ion batteries with superior volumetric capacity

Abstract

One of the key issues hampering the practical applications of powerful and thin sodium-ion batteries (SIBs) is low volumetric capacity. The purpose of this study is to report an innovative sputtering strategy to directly construct the vertically-aligned WS_2 columnar platelet film with low-tortuosity pores (VA/LT-WS_2) on an Al foil as an additive-free anode. Profiting from a 6 nm carbon overlayer on the top of the thickness-controllable film electrode (VA/LT-WS_2/C), the vertical feature of WS_2 and carbon layer enable high efficiency of ion and electron transportation pathways, respectively. The 2.8 μm VA/LT-WS_2/C film anode exhibits a high volumetric capacity of 1,339 mAh·cm^{-3} at 100 mA·g^{-1}, of which 30.2% is recorded when the current density gets a 50-fold increase from 100 to 5,000 mA·g^{-1}. Its gravimetric capacity of 366.8 mAh·g^{-1} is comparable to the reported WS_2 based anode materials for SIBs. Moreover, it is interesting to note that the discontinuous carbon layer (6 nm thickness) protects the presence of solid electrolyte interphase (SEI) layer from cracking caused by the volume expansion of WS_2 anode, and less than 16.7% volumetric capacity fading is presented after 300 cycles. It outperforms most of the recently reported outstanding SIBs anode materials. The SIB full cell exhibited a reversible volumetric capacity of 554 mAh·cm^{-3} at 50 mA·g^{-1} when the additive-free anode was applied in the VA/LT-WS_2/C // $Na_2V_3(PO_4)_3$/C full cell, demonstrating the potential of the physical sputtering VA/LT-WS_2/C for further battery development.

Keywords

Fast deposition, Vertically-aligned WS_2 platelet, Additive-free, Sodium ion battery anode, High volumetric capacity

1. Introduction

The new and strict requirements evoked by the continuous upward trend of portable devices and electronic products are the main driving force for developing rechargeable batteries for energy storage applications.[1-3] The sodium-ion batteries (SIBs) have received great attentions in recent years owing to the recoverable sodium reserves (natural abundance of 2.4 at. %) and the low exploitation cost, in comparison to the limited reserves of lithium in the earth crust (0.0065 at. %) for lithium-ion batteries (LIBs).[4,5] SIBs have the same operating principles as LIBs since sodium is a cognate element lithium. Nevertheless, one of existing obstructions to develop high-performance SIBs anode materials is the

sluggish kinetics for large size Na^+ (radius of 1.02 Å for Na^+ *vs* 0.76 Å for Li^+) diffusion into the laminar structural active materials, such as the graphite derivatives. The transition metal disulphides (TMDs, e.g., MoS_2, WS_2 and SnS_2), as 2D layered materials, have been identified as promising potential anode materials due to their weak van der Waals force between layers and large interlayer spacing (~6.2 Å) endowing them with excellent theoretical electrochemical intercalation of Na^+.[6,7] For the storage of intercalated sodium, the conversion reaction between Na^+ and TMDs could create the new reaction products of Na_2S and transition metal phases. Each transition metal ion can assist to 2~6 electrons, which is more than the case of intercalation reaction of Na/carbon system.[8,9] However, the anisotropic shape of TMDs and their horizontally stacked electrode results in a tortuous Na^+ diffusion pathway and poor electrical conductivity, resulting in significantly delaying the response time for electrochemical Na^+ intercalation.[10] Consequently, the vertically-aligned TMDs structures on the current collector can enable electron transport due to the higher conductivity inside of the (*xy*0) crystal plane and shortening the Na^+ diffusion pathway.[11-14]

The vertically-aligned TMDs on conductive substrates have achieved considerable success, but the low packing mass density of electrode active materials suppressed the SIBs' volumetric energy density.[15,16] Especially, due to the emergence of miniaturized wireless devices, such as micro-electromechanical systems, smart medical implants, thin and bendable personal electronics and so on, the thickness-controllable batteries with integrated power supplier are widely needed.[17-19] As one of the crucial components for the thickness-controllable battery, the packing thickness of electrode active materials should be tremendously reduced to micro- or even nano-scale as compared to common battery. The volumetric capacity (mAh cm^{-3}) has become to be a more important and reasonable evaluating criteria for thickness-controllable batteries than gravimetric capacity.[20-23] The most of current multistep chemical strategies in terms of the high cost and harmful-environment are not applicable for easily developing the high performance and thickness-controllable active materials for the thin film electrodes. [24-28] These two key issues of inapplicable synthesis strategies of active materials and the low volumetric capacity of electrode severely hamper the practical applications of powerful and thin SIBs. Besides, most conventional electrodes are currently facing the problems of the raised cost, the hindered diffusion paths of ions, and the reduced battery energy density due to addition of additives. Recently, physical approaches are widely studied to vertically-aligned active materials on the current collector. For example, graphite and $LiCoO_2$ particles were vertically-oriented on Cu foil by magnetic field force for LIBs.[29, 30] Vertically-aligned $Ti_3C_2T_x$ flakes on Al membrane were achieved by mechanical shearing of a discotic lamellar liquid-crystal phase of $Ti_3C_2T_x$ for supercapacitors.[31] These significant successes stimulate us

to explore an alternative straightforward and green synthetic strategy for TMDs thin film with open path for Na ions delivery, (*xy*0) crystal plane orientation for electron transport, high mass density of active material and a tight coupling interface between TMDs and current collector for charge-transfer, to finally achieve high volumetric capacity for the thickness-controllable SIBs anode without additives.

Herein, we propose a novel sputtering strategy to directly deposit the vertically-aligned WS_2 columnar platelet thin film with concomitant low-tortuosity pores (VA/LT-WS_2) at room temperature for the thickness-controllable SIBs anode. The excellent adhesion between the binder-free VA/LT-WS_2 films and the Al foil, directly constructed in the high-powered sputtering plasma environments, enables the structural stability of the electrode and the fast charge transfer at the interface. The corresponding Na storage mechanism for the WS_2 electrode can be proposed in the following insertion process:

$$WS_2 + xNa^+ + xe^- \rightarrow Na_xWS_2 \qquad \text{Equation (1)}$$

and the conversion reaction:

$$Na_xWS_2 + (4-x)\ Na^+ + (4-x)e^- \rightarrow 2Na_2S + W \qquad \text{Equation (2)}$$

, and the reversible reaction during the de-sodiation process can be described as:

$$Na_2S \rightarrow 2Na^+ + S + 2e^- \qquad \text{Equation (3)}$$

, which produced a theoretical gravimetric specific capacity of 432 $mAh \cdot g^{-1}$.[32-35] An ultrathin carbon (thickness of 6 nm) coated vertical WS_2 platelet thin film anode further suppressed the formation of excessive negative solid electrolyte interphase (SEI) during the charge/discharge process. We refer to the vertically-aligned WS_2 film with coated carbon layer as VA/LT-WS_2/C. The vertical columnar WS_2 film coated with 6 nm carbon layer, proposed as thin anode candidate for SIBs, delivers a remarkably high reversible volumetric capacity of 1,339 $mAh \cdot cm^{-3}$ at a current density of 100 $mA \cdot g^{-1}$ and only shows a total fluctuation of 16.7% after 300 cycles. The inherent pores around the vertically-aligned platelets in monolithic film can buffer the volume expansion during Na ion insertion/extraction processes. This construction approach of porous structure film enables the monolithic anode thickness to be tailored from a few microns to dozens of microns *via* simply changing the deposition time.

2. Experimental Section

2.1 WS_2 film deposition

The columnar WS_2 films on Al foil were fabricated by a sputtering technology equipped with WS_2 and C targets. The maximum area of the deposited film depends on the target size. The Al foil (40 mm L× 40 mm W× 0.015 mm thick, MTI Corporation), cleaned by acetone, was mounted on a rotated carousel in the vacuum chamber. Prior to the deposition, the Al foil substrates were bombarded by Ar plasma at

the pressure of 10 Pa for 30 minutes. For the deposition of the VA/LT-WS_2 film under the background pressure of 1.0×10^{-3} Pa, the source power density of WS_2 target was 0.115 W/mm^2, the Ar pressure was 1.3 Pa and bias voltage was -90 V. The WS_2 films with thickness of 2.8 were deposited for 48 minutes. The carbon coated WS_2 film on Al foil was fabricated as the carbon layer was deposited on the as-prepared WS_2 film surface by sputtering the carbon target for 5 minutes under the Ar pressure of 0.3 Pa and bias voltage of -90 V. The loading mass of WS_2 was calculated by weighing the cleaned Al foil before and after the WS_2 film deposition.

2.2 Synthesis of $Na_3V_2(PO_4)_3$/C

0.06 M NH_4VO_3 was completely dissolved in a 0.05 M citric acid solution under constant stirring, which resulted in a gradual change in colour from orange-red to dark blue. This was followed by the sequential addition of 0.045 M Na_2CO_3 and 0.09 M $NH_4H_2PO_4$. The above solution was transferred into a Tefon-coated hydrothermal container and kept at 180 °C for 24 h. The gel-like resultant was vacuum-dried until formation of xerogel. The xerogel was grinded to fine powder, then annealed at 800 °C for 8 h under Ar atmosphere [8].

2.3 Material characterization

The morphologies of VA/LT-WS_2 and VA/LT-WS_2/C were investigated by a field emission scanning electron microscopy (FESEM, JSM-7001F). The film thickness can be measured from its cross-section by FESEM. The phase structure of the films was characterized by an X-ray diffraction (XRD, Rigaku-G2005304) using Cu K_α radiation. The Raman spectrum was analysed using a Raman microscope (Thermo Scientific, DRX) with an excitation wavelength of 532 nm. The porous structure and the specific surface area of film was evaluated using the nitrogen (N_2) adsorption-desorption measurement apparatus (TriStar 3000 V6.07A instrument). The Brunauer-Emmett-Teller (BET) and Barrett-Joyner-Halenda (BJH) models were used to determine the specific surface area and the pore size of the sample, respectively. The nanostructure of the film was observed by a high-resolution transmission electron microscope (HRTEM, JEM, ARM 200F) operating at 200 kV, attached by energy dispersive X-ray spectroscopy. The specimens for HRTEM analysis were prepared by focused ion beam system (FIB, JEOL, JIB-4600F). The adhesion of the VA/LT-WS_2 and VA/LT-WS_2/C film on Al foil was evaluated using a custom-made bending tester. The films were subjected to 60° bending for 100 cycles at a rate of 1.0 Hz.

2.4 Electrochemical test

Electrochemical measurements were carried out using CR2032 coin-type cells. The VA/LT-WS_2 and VA/LT-WS_2/C film on Al foil were directly used as the anode electrode. It was prepared by directly

cutting the foil into disks (Φ14 mm) without any conductive additive or binder. The coin cells were assembled in an Ar-filled glove box ([O_2]<1 ppm, [H_2O]<1 ppm). Sodium metal was used as both the counter and reference electrodes. Glass fibre was used as separator. The electrolyte was 1.0 M $NaClO_4$ dissolved in propylene carbonate (PC) with 5.0 wt. % fluoroethylene carbonate (FEC) as additive. Cyclic voltammograms (CVs) and galvanostatic tests were performed at 0.2 $V \cdot s^{-1}$ between 0.01 and 3.0 V using a WBCS battery test system. The alternating-current (AC) impedance spectrum was measured in the frequency range of 100 kHz-0.01 Hz. A SIB full cell was assembled using VA/LT-WS_2/C as the anode and $Na_3V_2(PO_4)$/C as cathode. The voltage window was adjusted to 1.0~3.25 V and the mass loading ratio of the anode and cathode as 1:3 for the full cell.

3. Results and discussions

The WS_2 thin films were deposited on an Al foil in the carefully-controlled sputtering plasma environment (see the experimental section). However, the possible problem originating from direct deposition of separated columnar platelets is lattice mismatch between WS_2 active material and Al foil substrate and the limited contact area between them. These issues will cause off-pilling of active materials from the substrate when the mechanical strain increased during repeated insertion/extraction process. 100 times' bending test was performed to qualitatively evaluate the mechanical adhesion between the as-deposited WS_2 thin film and the Al foil current collector. The digital image of the bended electrode is shown in **Figure 1**a. The intact feature of the bended electrode revealed the strong interface coupling of the bottomed WS_2 layer and the Al foil, which is crucial to ensure a good structural stability towards long-term cycling performance. X-ray diffraction (XRD) examination was carried out to identify the crystal structure of the typical VA/LT-WS_2/C thin film electrode. As illustrated in **Figure 1**b (bottom), apart from the diffraction peaks from the electron current collector of Al foil, the peaks associated with (100) preferred orientation (located at 33.5 °) and concomitant (110) orientation (located at 59.7 °) of the *hcp*-WS_2 crystal edge plane were observed. This suggests that the *c* axis of the WS_2 crystal was parallel to the Al foil surface. The carbon coated layer was further examined by Raman spectra, as shown **Figure 1**b (top). The Raman peak located at 1365 cm^{-1} corresponds to the breathing mode of D band, and the one at around 1598 cm^{-1} is derived from the bond stretching of sp^2 carbon (G band). The low I_D/I_G intensity ratio of 0.56 suggests the relatively high degree of the sp^2 content of the carbon layer, which would increase the electrical conductivity.[36] In addition, two Raman peaks at around 352 cm^{-1} (E^1_{2g} mode) and 418 cm^{-1} (A_{1g} mode) correspond to *hcp*-WS_2, in a good agreement with XRD

characterization.[37] The absence of Raman peaks at 260 cm^{-1} and 808 cm^{-1} confirms no formation of tungsten carbide by-product at the interface between WS_2 and C layers.

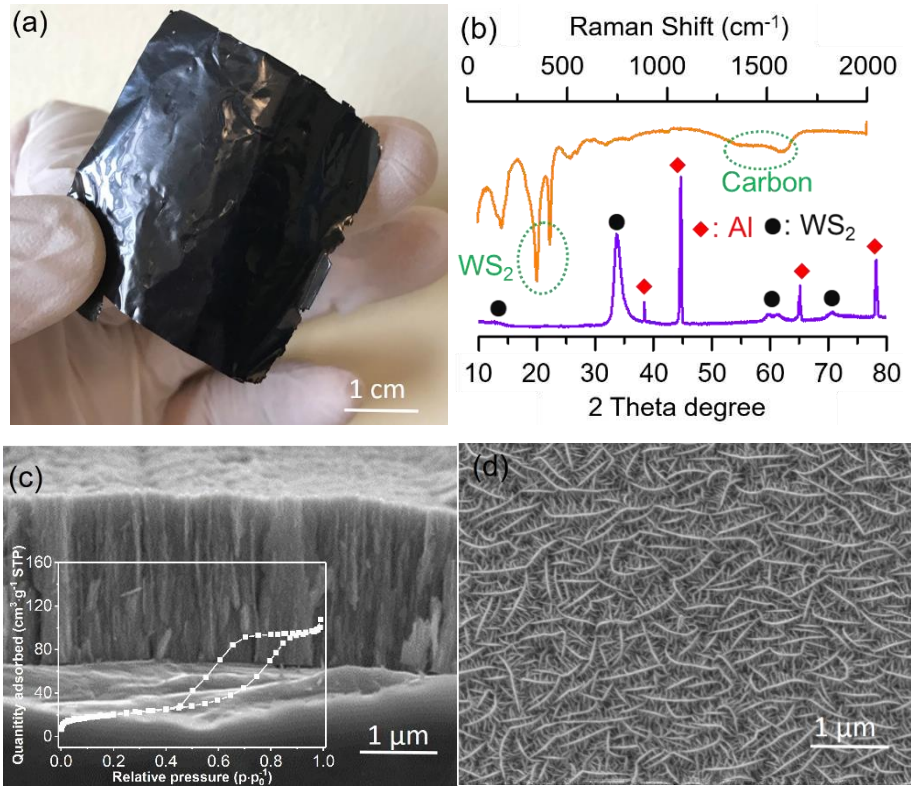

Figure 1 As-deposited 2.8 μm VA/LT-WS_2/C thin film on the Al foil current collector: (a) digital image of electrode after 100 times' bending test, (b) XRD and Raman spectra, (c) cross-sectional and (d) surface FESEM images. The inset curve in (c) is the nitrogen adsorption-desorption isotherm of the VA/LT-WS_2/C thin film.

The cross-sectional and surface morphologies of the VA/LT-WS_2/C thin film anode were investigated by FESEM (**Figure 1**c-d). The thickness of film deposited for 48 minutes was 2.8 μm (**Figure 1**c). WS_2 columnar platelets with a fully consistent height of 2.8 μm are clearly observed on the Al foil (**Figure 1**c). All the film platelets exhibit less than 100 nm thickness and a high aspect ratio, as observed from the surface morphology of the VA/LT-WS_2/C thin film (**Figure 1**d). To shed light on the interior structure of VA/LT-WS_2/C film, the nitrogen adsorption-desorption isotherm analysis was performed and the result is shown in the inset of **Figure 1c**. The typical hysteresis loop (P/P_0 in the range of 0.4~0.9), specific surface area of 53.7 $m^2 \cdot g^{-1}$ and the peak value of 12.9 nm in the pore width distribution curve (**Figure S1**) suggest the mesoporous feature of the low-tortuosity pore structure of WS_2 film. The ultrathin carbon layer coated on the WS_2 film did not bury the abundance of pores and edge features (**Figure 1**d). Moreover, the thimbleful amount of this ultrathin carbon layer allows us to evaluate the

mass loading of electrode based on WS_2 active material film only. The mass per unit area of WS_2 is about 1.02 $mg \cdot cm^{-2}$ (the average deviation of 0.01 $mg \cdot cm^{-2}$) and the tapping density (density (D_t)) is 3.65 $g \cdot cm^{-3}$ (~48.7% of the natural WS_2). Thus, the estimated porosity over 50% of VA/LT-WS_2 array is expected to provide sufficient access for the electrolyte throughout the active materials characterized by low-tortuosity pore structure.

Previously, most of vertically-aligned TMDs sheets were synthesised *via* the complicated and multistep chemical strategies.[9-11] In comparison, by optimizing deposition experiment parameters (bias voltage, Ar pressure and sputtering power source density) in this work, the high packing mass density of vertically-aligned WS_2 platelet film for the additive-free anode can be directly and easily constructed on the current collector using the sputtering technology. And the growth velocity of WS_2 columnar platelets reached up to ~58 nm/min, which was much faster than that of the reported atomic layer deposition method.[38-40] The procedure is schematically outlined in **Figure 2**. High vacuum condition (1.0×10^{-3} Pa) was achieved before WS_2 film deposition to avoid any influence of residual species on purity of sputtering plasma in the chamber. The vertically-aligned WS_2 films on the Al foil (**Figure 1**c-d) were deposited when the high energy sputtering plasma was produced in the Ar ion atmosphere under the aforementioned experiment conditions. The ultrathin carbon layer can be easily coated on the as-deposted WS_2 thin film when it was located in the carbon plasma. For tailoring WS_2 film thickness, the vertically-aligned WS_2 thick film with thickness of 16.0 μm was obtained (**Figure S2** and **Figure S3**) when the depostion time was extended to 288 minutes in the WS_2 plasma and other conditions maintained constant. This thick WS_2 film still possesses the same columnar platelet and porosity characterization. The influence of the WS_2 target's sputtering energy on film stucture and performace was also investigated. When the sputtering source power density of WS_2 target was increased from 0.115 $W \cdot mm^{-2}$ to 0.20 $W \cdot mm^{-2}$, the resulting WS_2 thin film still has VA-structure but it consists of coarse columnar platelets and enlarged pores (**Figure S4**). As a consequence, the vertically-aligned WS_2 structure can be easily tailored by carefully tuning experiment parameters.

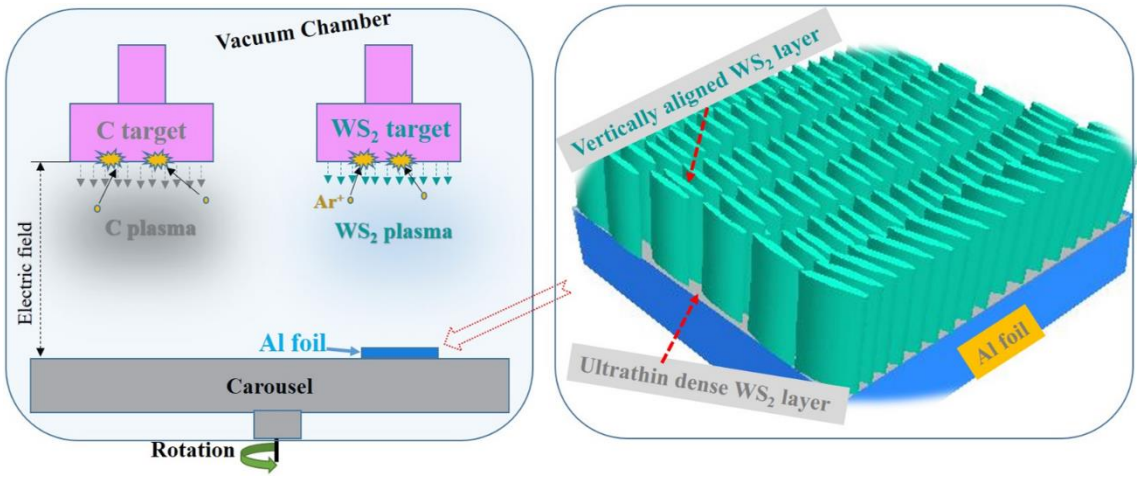

Figure 2. Schematic illustration of the direct depostion of VA/LT-WS_2/C thin film on the Al foil current collecter.

The nanostructure of the VA/LT-WS_2/C thin film electrode with tapping density was further analyzed. A FIB sample of the cross-sectional VA/LT-WS_2/C (2.8 μm) thin film electrode was prepared with two protection layers of the first-deposited Ir and the second-deposited mixture of Pt and C to avoid any damage in the FIB process (**Figure S5**). TEM image of the representative zone of the cross-sectional VA/LT-WS_2/C thin film is shown in the **Figure 3**a. It can be seen that the columnar platelets possess the vertical alignment and porous features. This structure is ascribed to rapid growth of the separated platelets throughout the film in the high energy sputtering plasma environment. In comparison to the homogeneous elemental maps of the Al foil, the fluctuating distribution W and S elements further demonstrates the porosity feature throughout the columnar platelet film (**Figure S6**). These nanopores decreased the tapping density of the VA/LT-WS_2/C thin film anode, but they could act as a buffer zone for volume expansion of WS_2 platelets during sodiation/de-sodiation process. The corresponding selected area electron diffracton (SAED) pattern of the representative zone of thin film presents the hexageonal structure of WS_2 (the inset of **Figure 3**a). The clear (100) and (110) rings, well consistent with the XRD results, are the straight evidences for the identification of the WS_2 crystal structure with *c* axis parallel to the Al foil current collecter surface. **Figure 3**b exhibits the cross-sectional HRTEM image with high resolution of the VA/LT-WS_2/C thin film at WS_2/Al interface. It can be found that the firstly-formed dense basal orientation crystalline WS_2 layer with thickness of ~22 nm can act as an intermediate transition layer to enable the full contact between WS_2 film and Al foil. In the sequential depostion process in high energy sputtering conditions, the nanosturcture evloved into a vertically-aligned WS_2 crystal characterized by columnar platelets and a number of concomitant pores from the initial parallelly-aligned WS_2 crystal planes (**Figures 3**b,c). The HRTEM image of columnar platelets (see **Figure 3**c)

exhibits the 6.2 Å interlayer space corresponding to the vertically-aligned (002) plane of *hcp*-WS_2, in good line with the XRD pattern. The WS_2 thin film composed of columnar platelets and a number of pores can be created with insufficient bulk diffusion and sufficient surface diffusion of sputtered adatoms during the film growth process. The high target sputtering power and low resputtering degree in the sputtering plasma produced a high growth velocity in the [*hk0*] direction of the sputtered adatoms to finally form the columnar platelets. An ultrathin discontinuous carbon layer (thickness of 6 nm) was coated on the columnar platelet top of the VA/LT-WS_2/C thin film (**Figure 3**d, **Figures S7, S8**). The measurement criteria of the deposited carbon layer thickness was given in supplementary information (**Figure S9**). The pores of the VA/LT-WS_2/C thin film were't clogged by the carbon layer. A part of carbon can diffuse into the VA/LT-WS_2/C thin film during the carbon deposition process(**Figure S7**). The specific purpose of covering the ultrathin carbon on the WS_2 film surface is to improve electrical conductivity in consideration of instrinsic semiconductive characteristics of WS_2. The representative single vertially-aligned columnar platelet of WS_2 crystal is shown in **Figure 3**e. The columnar platelets are expected to act as the direct channel for efficient delivery of Na ions and rapid electron transport to the current collector. Moreover, the discontinuous carbon layer is also expected to ease the loss of the sulfide and prevent consumption of Na ions due to the formation of surface-electrolyte interphase (SEI) and other side reactions in the charging and discharging process of anode.[41, 42]

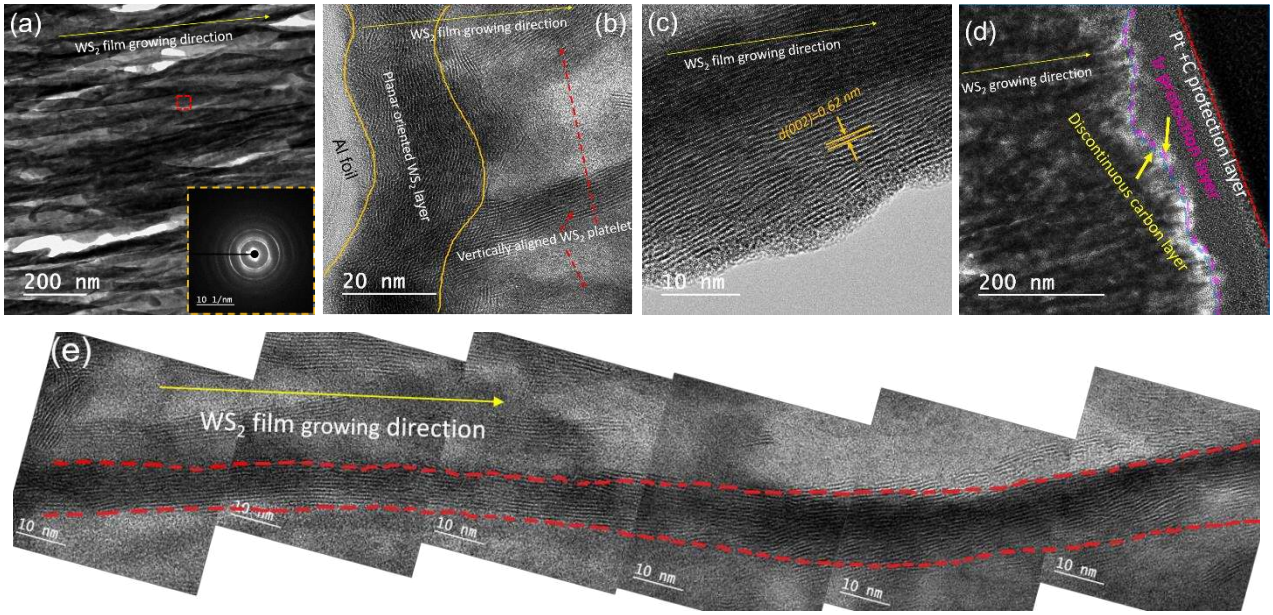

Figure 3 (a) TEM image of representative zone with inset of selected area electron diffracton (SAED) pattern of the cross-sectional VA/LT-WS_2/C thin film anode, and high resolution TEM images (b) at WS_2/Al interface and (c) of representative zone from the selected red square in (a), and (d) the distribution

of the discontinuous carbon layer at the subsurface zone and (e) the representative single vertially-aligned columnar platelet of WS_2 crystal.

With special emphasis on development of anodes for practical applications of thin and powerful SIBs, the 2.8 μm VA/LT-WS_2 and VA/LT-WS_2/C thin film anodes were mainly assessed in this study. To evaluate the Na ion insertion/extraction behavior of VA/LT-WS_2 and VA/LT-WS_2/C thin film anodes, their electrochemical activities were investigated *via* cyclic voltammentry (CV) measurements at 0.2 $mV \cdot s^{-1}$ over the potential range of 0.01-3.0 V. The recorded curves are plotted in **Figures 4**a-b. Three cathodic peaks located at around 0.89, 0.51 and 0.098 V and a prominent anodic peak at 1.87 V during the first cycle for both VA/LT-WS_2/and VA/LT-WS_2/C thin films. In detail, the peak appearing in the vicinity of 0.89 V can be attributed to the Na^+ intercalation into WS_2 interlayer space, forming Na_xWS_2, accompanied by the phase transformation from the 2*H* to the 1*T* structure of Na_xWS_2, as illustrated in Equeation (1).[37, 38] The peak at 0.51 V is due to the electrochemical conversion reaction with the formation of Na_2S, as illustrated in Equation (2). In the anodic scans, the pronounted peak at 1.87 V indicates the Na extraction from Na_2S, as illustrated in Equation (3). The change of crystal structure the VA/LT-WS_2/C electrode upon Na^+ intercalation was determined by ex-situ XRD, which demonstrated the reversible intercalation/deintercalation process over the operated potential range. (**Figure S10**). The cathodic peak at 0.098 V, which disappeared after first cycle, can be associated with SEI layer formation.[27, 28, 43, 44] Remarkably, this peak intensity of VA/LT-WS_2/C thin film anode was reduced in comparision to the VA/LT-WS_2, indicating that the simple coating of discontinuous carbon layer on the top of vertically-aligned WS_2 platelets can effectively suppress the growth of the excessive irreversible SEI layer.

Figures 4c-d compare the galvanostatic charge/discharge profiles of both VA/LT-WS_2 and VA/LT-WS_2/C thin film anodes recorded for the first five cycles at a current density of 500 $mA \cdot g^{-1}$. In the first charge/discharge cycle, the coulombic efficiency (CE) of the VA/LT-WS_2/C thin film anodes is 72%, superior to that of VA/LT-WS_2 thin film anode (64%), which can be ascribed to SEI layer suppression by carbon layer. And the first discharge processes of WS_2 films exhibit the correlative plateau regimes (at around 0.85, 0.50 and 0.21 V), which are identified to the first discharge CV profile, indicating the insertion, conversion and SEI formation of WS_2 anode.[34] For the VA/LT-WS_2/C thin film anode, the charge/discharge curves after first scanning became much consistent and gravimetric specific capacity reaches 277 $mAh \cdot g^{-1}$ with an improved CE of ~95%, which was much better than the VA/LT-WS_2 thin film anode. Thus, it is evidenced that both VA/LT-WS_2 and VA/LT-WS_2/C thin film anodes show less clear voltage plateaus, suggesting that the vertical structure creates efficient Na^+ diffusion channels.

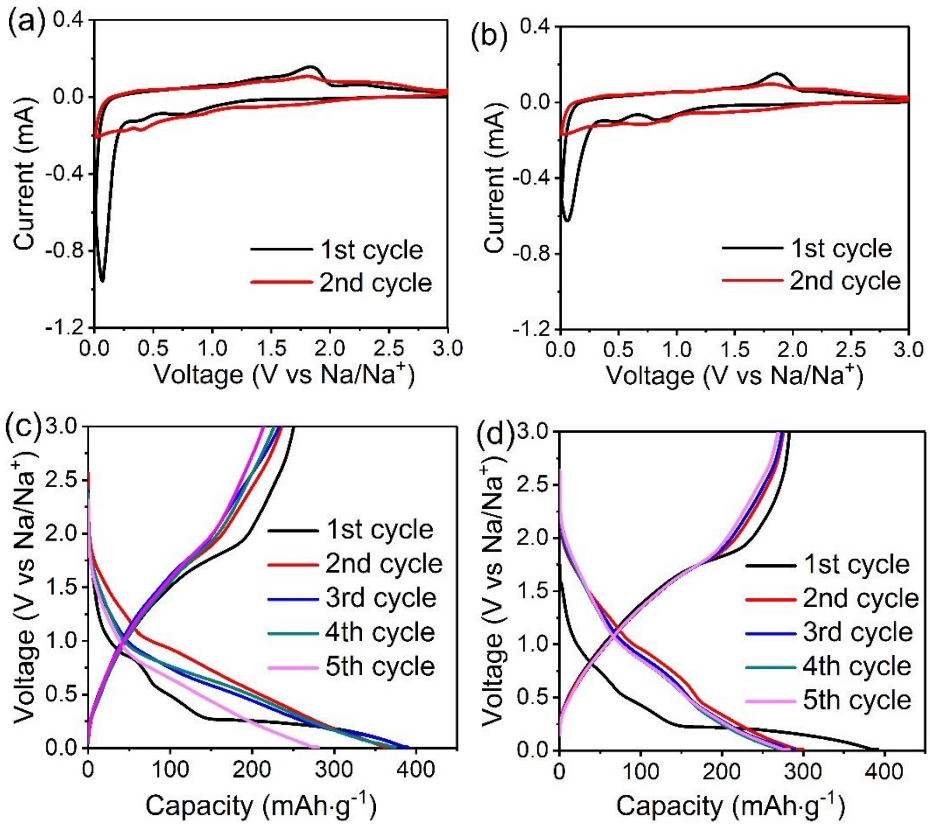

Figure 4 First two cycles voltammogram curves at a scanning rate of 0.2 $mV \cdot s^{-1}$ of (a) the VA/LT-WS_2 and (b) VA/LT-WS_2/C thin film anodes, and charge/discharge curves of the first five cycles at 500 $mA \cdot g^{-1}$ for the (c) the VA/LT-WS_2 and (d) VA/LT-WS_2/C thin film anodes.

The rate capacities of the VA/LT-WS_2 and VA/LT-WS_2/C thin film anodes are shown in **Figure 5**a. The new half cells were tested for five cycles at current densities ranging from 100 to 5,000 $mA \cdot g^{-1}$. When the gravimetric specific current ramp up stepwise from 100 to 200, 500, 1,000, 2,000 and 5,000 $mA \cdot g^{-1}$, the average gravimetric specific capacities of VA/LT-WS_2 anode / VA/LT-WS_2/C anode are 231.4/343.2, 156.6/302.3, 118.7/279.5, 91.3/242.6, 36.6/187.2 and 8.6/103.8 $mAh \cdot g^{-1}$, respectively. The volumetric capacity (VC) can be derived from the following formula:

$$C_v = C_g * D_t$$

where C_v is the VC ($mAh \cdot cm^{-3}$), C_g is the spesific capacity ($mAh \cdot g^{-1}$) and D_t is the density ($g \cdot cm^{-3}$) of the active materials on the electrode. Note that the corresponding impressive volumetric capacities of 844.6/1,252.7, 571.6/1,103.4, 433.3/1,020.2, 333.4/885.5, 134.0/683.3 and 31.4/378.9 $mAh \cdot cm^{-3}$ were obtained, respectively. Obviously, the high VC of the anode was ascribed to the high tapping density of 3.65 $g \cdot cm^{-3}$ for the vertically-aligend WS_2 active materials. Moreover, the VA/LT-WS_2/C thin film anode displays superior rate performance to the VA/LT-WS_2 thin film anode. Besides the positive contribution of carbon layer on SEI layer suppression, the carbon layer could also enhance the conductivity of VA/LT-

WS_2/C thin film anode. The aforementioned analysis results of low ratio of I_D/I_G (Raman spectrum) of 0.56 could verify the relatively high degree of graphitization of the carbon layer which has inherent high electrical conductivity. To further demonstrate this point, the measurement of electrochemical impedance spectroscopy (EIS) of electrodes was performed, and the Nyquist plots of VA/LT-WS_2 and VA/LT-WS_2/C thin film anodes are shown in **Figure 5**b. The Nyquist plots consist of two typical regions: the single depressed semicircle corresponding to the charge transfer resistance in the high-medium frequency region and an inclined line corresponding to the Na ion diffusion into the WS_2 active materials in the low frequency region (Warburg).[45, 46] The two electrodes show a similar and high slope of the inclined lines in the Warburg region, demonstrating the significant enhancement of the Na^+ ion diffusion in the vertical columnar platelets. Obviously, the carbon coated VA/LT-WS_2/C thin film features a much smaller semicircle diameter than that of VA/LT-WS_2 thin film, indicating a lower charge-transfer resistance that arises from the high electrical conductivity of the carbon layer.

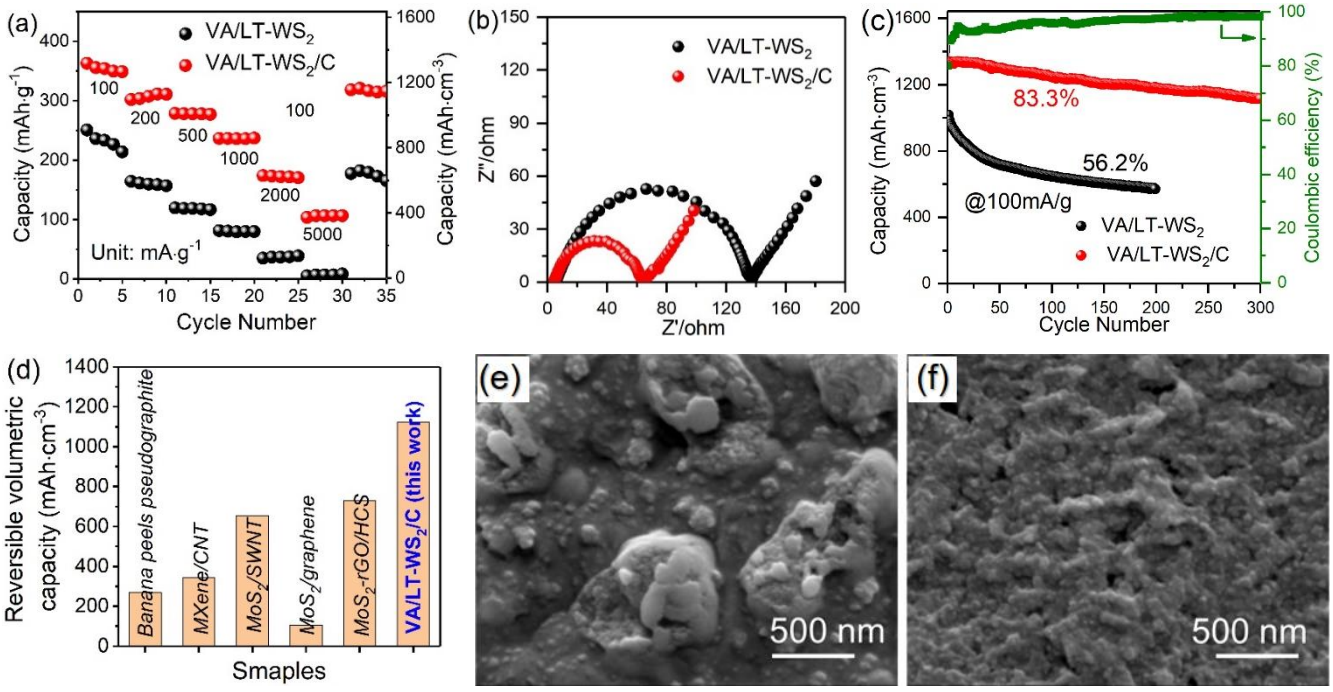

Figure 5 (a) Rate performances of VA/LT-WS_2 and VA/LT-WS_2/C thin film anodes at current density from 100 to 5,000 $mA \cdot g^{-1}$, (b) Nyquist plots after runing 10 cycles of the VA/LT-WS_2 and VA/LT-WS_2/C thin film anodes at 100 $mA \cdot g^{-1}$, (c) cycling performance of VA/LT-WS_2 and VA/LT-WS_2/C thin film anodes at 100 $mA \cdot g^{-1}$, (d) the reversible volumetric capacity of VA/LT-WS_2/C compared with the previous studies on different electrodes, and surface morphology FESEM images of (e) VA/LT-WS_2 and (f) VA/LT-WS_2/C thin film anodes after 200 and 300 cycles at 100 $mA \cdot g^{-1}$, respectively.

The cycling performances of VA/LT-WS_2 and VA/LT-WS_2/C thin film electrodes were evaluated at a current density of 100 mA·g^{-1} (**Figure 5**c). It can be found that the VA/LT-WS_2 thin film electrode presents ~56.2% capacity retention after 200 cycles. While the volumetric capacity of VA/LT-WS_2/C thin film electrode is declined from 1,339 mAh·cm^{-3} (gravimetric capacity of 366.8 mAh·g^{-1}) to 1,122 mAh·cm^{-3} (gravimetric capacity of 307.4 mAh·g^{-1}) after the 300th cycle (corresponding to 83.3% of the initial capacity). The initial coulombic efficiency (CE) of VA/LT-WS_2/C is around 79.9%, after which the CE remarkably increases and then gradually reaches 98.4%, probably ascribing to electrochemical activation of electrode [8]. The volumetric capacity is the most relevant figure-of-merit critical in practical application for thin and powerful SIBs as compared to gravimetric specific/areal capacity.[17-20] As far as we know, these are no previous reports on sputtering deposited TMDs film as anode materials or volumetric capacities of any other WS_2 active material for SIBs anodes.[26, 47] The volumetric capacity of the VA/LT-WS_2/C electrode outperforms most of the recently reported outstanding anode materials for SIBs, no matter the common or thin-film SIBs anodes (shown in **Figure 5**d and **Table. S1**). [10, 15, 48-50] Besides, the gravimetric capacity of VA/LT-WS_2/C electrode is comparable to the reported WS_2 based anode materials for SIBs.[14,27,28,33] It demonstrates the potentially rewarding performance of the sputtered VA/LT-WS_2/C thin film anode can be achieved by carefully tailoring the film structure. Besides, another important advantage of the directly sputtered VA/LT-WS_2/C thin film on Al foil as anode material is the simplified assembly steps (listed in **Table. S1**) which does not need any binder. For the as-deposited thick VA/LT-WS_2/C film anode with thickness of 16.0 μm in this study, it can still anchor onto the current collector surface well (**Figure S2**) and maintain the high volumetric capacity of 914.5 mAh cm^{-3} (gravimetric capacity of 250. 7 mAh·g^{-1} and areal capacity of 1.46 mAh·cm^{-2}) at a current density of 100 mA·g^{-1} (**Figure S11**). The galvanostatic intermittent titration technique (GITT) was further employed to investigate the Na ion diffusivity and understand the underlying mass diffusion kinetics of the VA/LT-WS_2 electrode. The result (as presented in **Figure S12**) demonstrates that the deposited porous and columnar WS_2 film has the higher Na ion transportation that is almost one order of magnitude higher than that of slurry casted WS_2 electrode. The morphology of 2.8 μm VA/LT-WS_2 thin film anode displays several bulge after running 200 cycles (**Figure 5**e), while the VA/LT-WS_2/C thin film anode after running 300 cycles reveals a flat surface with distinguishable SEI layer (**Figure 5**f). The results suggested that the carbon layer can serve as a conductive layer to facilitate electron transport and also a protection layer to maintain a continuous SEI layer. The serving VA/LT-WS_2/C electrode still maintained the vertically-aligned array structure (**Figure S13**). This enables vertically-orientated WS_2 platelets to invariably immobilize on the current collector of Al foil and stable performance during the long-term

sodiation/de-sodiation processes. In addition to the role of the thin carbon overlayer, the moderate porous feature of the WS_2 columnar platelets played a crucial factor to alleviate electrode deterioration.

It was generally accepted that high porosity of the anode active material provided enough space for the free volume expansion during Na ion insertion/extraction, which can well mitigate mechanical stress to stabilize electrode structure.[52-54] However, in our case, another high-porous VA/LT-WS_2/C thin film displayed rapid capacity fading (**Figure S14**). The porosity feature of the VA/LT-WS_2/C thin film anode was evidenced by observing their internal morphology (**Figure S15**). Significantly, the high-porous VA/LT-WS_2/C thin film anode exhibited huge surface cracks after running 200 cycles (**Figure S16**). Presumably, the excessive porosity may lead to electrode collapse because the separated coarse WS_2 columnar platelets with weak strength experienced structural destruction. Besides, the deposited dense WS_2 film was easily peeling off from the flexible Al current collector due to the residual stress and low flexibility of the dense film (**Figure S17**), which can't either serve as the additive-free anode for SIBs.

This WS_2 thin film active material with vertically-aligned porous and columnar structure was rapidly and easily fabricated on the electron collector of the Al foil *via* an attractive sputtering deposition strategy, and it had impressive cycling stability and great volumetric capacity *via* covering carbon thin layer. The advantages of this innovative sputtering strategy can be ascribed to: (i) the interfacial dense crystalline WS_2 layer (~22 nm) enabled strongly coupling and invariable immobilization of WS_2 and Al foil current collector to avoid the easily exfoliation of platelets in the root by the electrode deformation as verified by the bending test, (ii) the vertical WS_2 platelet film with low-tortuosity open channles ensured an optimal pathway for fast transport of the electrode ions which indeed led to the significantly-improved rate performance, especially in the relative dense and large mass loading electrode,[11, 13, 55-58] (iii) the abundance of tailored pores with low-tortuosity feature could not only enhance the affinity of the electrolyte and increase the contact areas between WS_2 platelet active material and the electrolyte, leading to an enhanced Na ion accessibility and further reduction of Na ion diffusion distance, but also buffer the volume expansion during Na ion insertion/extraction processes, being beneficial for improving the structural stability, and (iv) the tightly carbon overlayer on the top of WS_2 columnar platelets can suppress the formation of excessive negative SEI layer and reduce the charge-transfer resistance at electrolyte/electrode interface. As a result, the rapid and easy preparation strategy of sputtering further implies that this kind of VA/LT-WS_2/C thin film is a highly competitive candidate for anode of SIBs.

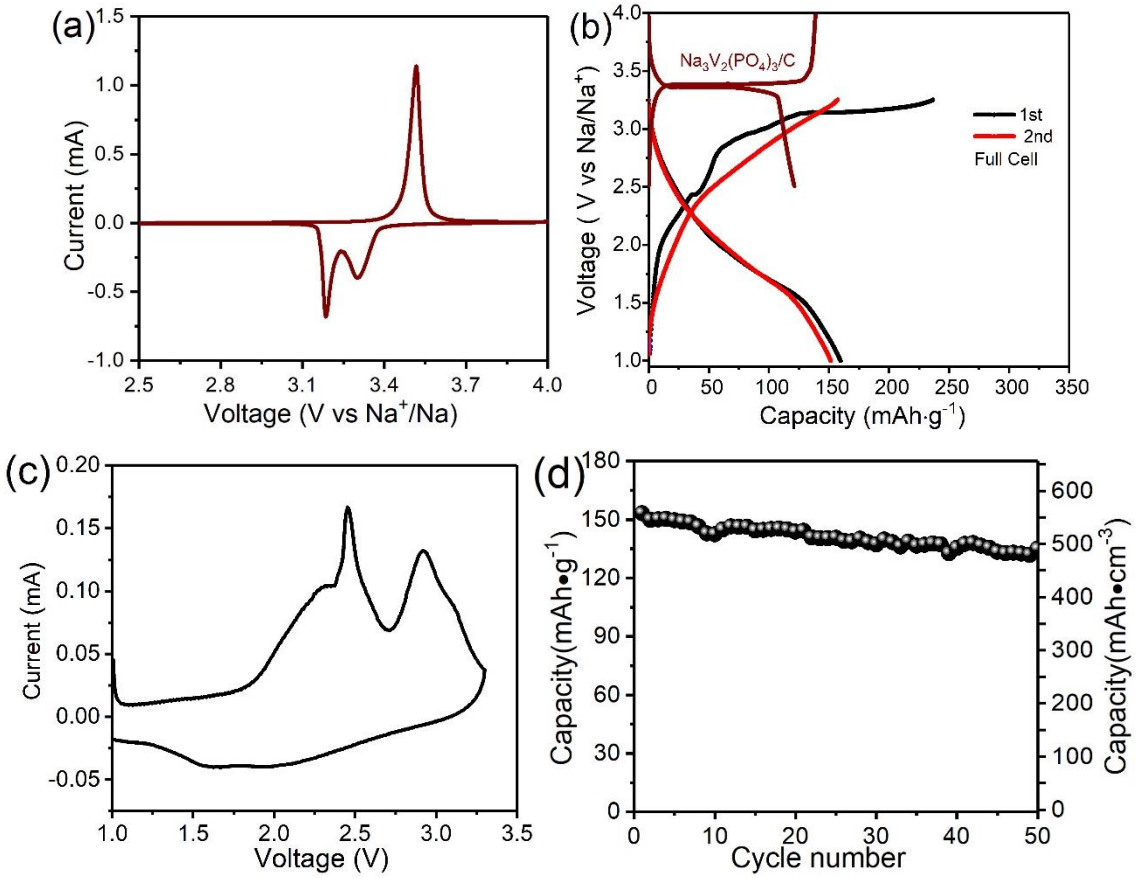

Figure 6. (a) CV curve of $Na_3V_2(PO_4)_3$/C at a scanning rate of 0.1 mV·s^{-1}, (b) charge/discharge profiles of $Na_3V_2(PO_4)_3$/C half cells and VA/LT-WS_2/C // $Na_3V_2(PO_4)_3$/C full cell at a current density of 50 mA·g^{-1}, (c) CV curve of the VA/LT-WS_2/C // $Na_3V_2(PO_4)_3$/C full cell at a scan rate of 0.05 mV·s^{-1} and (d) cycling performance of VA/LT-WS_2/C // $Na_3V_2(PO_4)_3$/C full cell at a current density of 50 mA·g^{-1}.

The physical sputtering VA/LT-WS_2/C, with impressive electrochemical performance, is a promising strategy for SIBs application. Herein, a SIB full cell was assembled using VA/LT-WS_2/C as the anode and Na_3V_2 $(PO_4)_3$/C as cathode.[8] **Figures 6**a,b present the CV curve of $Na_3V_2(PO_4)_3$/C at a scanning rate of 0.1 mV·s^{-1} and the charge/discharge profile in the same voltage window as the CV curve, respectively. The sharp oxidation peak at ≈3.52 V in $Na_3V_2(PO_4)_3$/C CV curve is assigned to the V^{4+} to V^{3+} redox potential which is essentially related to the phase transformation from $Na_3V_2(PO_4)_3$ to $NaV_2(PO_4)_3$.[51] The split reduction peaks may be accompanied by the stepwise intercalation of Na^+ from $NaV_2(PO_4)_3$ to $Na_2V_2(PO_4)_3$ then to $Na_3V_2(PO_4)_3$.[8] The charge/discharge profile shows the charge capacities of 121.2 and 139.1 mAh·g^{-1} with the potential plateau of ≈3.46 V at the current density of 50 mA·g^{-1} (**Figure 6**b). The CV curve of the full cell was measured at a scanning rate of 0.05 mV·s^{-1} at the voltage window of 1.0 to 3.25 V (**Figure 6**c), and the result exhibits an operating voltage of ≈1.6 V. The

gravimetric capacity of full cell reaches 152 mAh·g^{-1} (volumetric capacity of 554 mAh·cm^{-3}) in the charge-discharge profile at a current density of 50 mA·g^{-1} (**Figure 6**b). The specific capacity is calculated based on the mass of the anode. The capacity can maintain 87.5 % of the initial performance after 50 cycles (**Figure 6**d), which demonstrates the potentiality of the physical sputtering VA/LT-WS_2/C monolithic electrode on Al foil as anode active material for SIBs. On basis of this successful exploration of physical sputtering strategy, other TMDs (like SnS_2, MoS_2, $MoSe_2$, and so on) sputtering electrodes would be further constructed to achieve the possible much better performance.

4. Conclusion

In summary, we demonstrated an innovative strategy of constructing the vertically-aligned WS_2 columnar platelet thin film (with/without carbon coated layer) on an Al foil as an additive-free anode material for thickness-controllable sodium ion batteries (SIBs) through sputtering technology. The continuous vertical alignment and low-tortuosity pore structure facilitated the transport of ions in the anode, and the ultrathin carbon layer (6 nm) promotes conductivity of electrode and formation of flat solid electrolyte interphase layers, thereby resulting in the high and stable rate performance: the volumetric capacity of 1,339 mAh·cm^{-3} (gravimetric capacity of 366.8 mAh·g^{-1} and areal capacity of 0.374 mAh·cm^{-2}) at 100 mA·g^{-1} and less than 16.7% capacity fading after 300 cycles for the 2.8 μm VA/LT-WS_2/C thin film electrode. Moreover, the excellent adhesion between WS_2 film active material and Al foil without binder is beneficial for the anchoring of the WS_2 columnar platelet film on the current collector. This VA/LT-WS_2/C thin film electrode outperforms most of the recently reported outstanding materials for SIBs anode. The SIB full cell composed of the VA/LT-WS_2/C anode and a $Na_3V_2(PO_4)_3$/C cathode exhibited a volumetric capacity of 554 mAh·cm^{-3} at 50 mA·g^{-1} and maintained 87.5 % of the initial performance after 50 cycles. In addition to the natural abundance and low cost of Na, this cost efficiency physical sputtering construction technology for vertically-aligned and thin transition metal disulphides (TMDs) film on current collection is an innovative way to further promote the development of rechargeable batteries with thickness-controllable and additive-free anode electrodes.

Acknowledgements

The authors are grateful for the financial support provided by Engineering and Physical Sciences Research Council (EPSRC, Grant No. EP/R00496X/1) in the United Kingdom, and Natural Science Foundation of China (CN) (Grant No. 51505465 and 51575508). We also would like to thank the helpful FIB and TEM tests and the constructive suggestions by Mr. John Harrington, Mrs. Zebeada Aslam and

Mr. Satuart Micklethwaite from Leeds Electron Microscopy and Spectroscopy Centre (LEMAS), University of Leeds.

Appendix A. Supporting information

Supplementary data associated with this article can be found in the online version at //

Conflict of Interest

The authors declare no conflict of interest.

Data availability

The raw/processed data required to reproduce these findings cannot be shared at this time due to technical or time limitations.

Referencs

[1] B. Dunn, H. Kamath, J.-M. Tarascon, Electrical energy storage for the grid: a battery of choices, **Science** 334(2011) 928-935.

[2] S. Chu, A. Majumdar, Opportunities and challenges for a sustainable energy future, **Nature** 488(2012) 294-303.

[3] K, Shi, C. Lai, X.J. Liu, Y.P. Wei, W. Lv, J.S. Wang, J. Li, C.L. Yan, B.H. Li, Q. H. Yang, F.Y. Kang, Y.B. He, $LiNi_{0.8}Co_{0.15}Al_{0.05}O_2$ as both a trapper and accelerator of polysulfides for lithium-sulfur batteries, **Energy Storage Mater.** 17(2019) 111-117.

[4] Y.Y. Huang, Y.H. Zheng, F. Adams, W. Luo, Y.H. Huang, L.B. Hu, Electrode materials of sodium-ion batteries toward practical application, **ACS Energy Lett.** 3(7)(**2**018) 1604-1612.

[5] X.Y. Zheng, C. Bommier, W. Luo, L.H. Jiang, Y.N. Hao, Y.H. Huang, Sodium metal anodes for room-temperature sodium-ion batteries: Applications, challenges and solutions, **Energy Storage Mater.** 16(2019) 6-23.

[6] F. Klein, B. Jache, A. Bhide, P. Adelhelm, Conversion reactions for sodium-ion batteries, **Phys. Chem. Chem. Phys.** 15(2013) 15876-15887.

[7] M. Pumera, Z. Sofer, A. Ambros, Layered transition metal dichalcogenides for electrochemical energy generation and storage, **J. Mater. Chem. A** 2(2014) 8981-8987.

[8] J. Cabana, L. Monconduit, D. Larcher, M. R. Palacín, Beyond intercalation-based Li-ion batteries: the state of the art and challenges of electrode materials reacting through conversion reactions, **Adv. Mater.** 22(2010) E170-192.

[9] L. David, R. Bhandavat, G. Singh, MoS_2/graphene composite paper for sodium-ion battery electrodes, **ACS Nano** 8(2014) 1759-1770.

[10] P. Li, J. Y. Jeong, B. J. Jin, K. Zhang, J. H. Park, Vertically oriented MoS_2 with spatially controlled geometry on nitrogenous graphene sheets for high- performance sodium- ion batteries, **Adv. Energy Mater.** 8(2018) 1703300.

[11] H. Liu, D. W. Su, R. F. Zhou, B. Sun, G. X. Wang, S. Z. Qiao, Highly ordered mesoporous MoS_2 with expanded spacing of the (002) crystal plane for ultrafast lithium ion storage, **Adv. Energy Mater.** 2(2012) 970-975.

[12] D. W. Su, S. X. Dou, G. X. Wang, Ultrathin MoS_2 nanosheets as anode materials for sodium- ion batteries with superior performance, **Adv. Energy Mater.** 5(2015) 1401205.

[13] W. H. Ryu, H. Wilson, S. W. Sohn, J. Y. Li, X. Tong, E. Shaulsky, J. Schroers, M. Elimelech, A. D. Taylor, Heterogeneous WS_x/WO_3 thorn-bush nanofiber electrodes for sodium-ion batteries, **ACS Nano** 10(2016) 3257-3266.

[14] Y. Wang, D. Z. Kong, W. H. Shi, B. Liu, G. J. Sim, Q. Ge, H. Y. Yang, Ice templated tree-standing hierarchically WS_2/CNT- rGO aerogel for high- performance rechargeable lithium and sodium ion batteries, **Adv. Energy Mater.** 6(2016) 1601057.

[15] Y. P. Liu, X. Y. He, D. Hanlon, A. Harvey, J. N. Coleman, Y. G. Li, Liquid phase exfoliated MoS_2 nanosheets percolated with carbon nanotubes for high volumetric/areal capacity sodium-ion batteries, **ACS Nano** 10(2016) 8821-8828.

[16] Y. L. Ding, P. Kopold, K. Hahn, P. A. van Aken, J. Maier, Y. Yu, A lamellar hybrid assembled from metal disulfide nanowall arrays anchored on a carbon layer: in situ hybridization and improved sodium storage, **Adv. Mater.** 28(2016) 7774-7782.

[17] J. F. Oudenhoven, L. Baggetto, P. H. Notten, All- solid- state lithium- ion microbatteries: a review of various three- dimensional concepts, **Adv. Energy Mater.** 1(2011) 10-33.

[18] L.X. Liu, Q.H. Weng, X.Y. Lu, X.L. Sun, L Zhang, O.G. Schmidt, Advances on microsized on-chip lithium-ion batteries, **Small** 13(2017) 1701847.

[19] H.S. Lee, S.T. Kim, K.B. Kim, J.W. Choi, Scalable fabrication of flexible thin-film batteries for smart lens applications, **Nano Energy** 53(2018) 225-231.

[20] Y. Gogotsi, P. Simon, True performance metrics in electrochemical energy storage, **Science** 334(2011) 917-918.

[21] J. M. Luo, X. Y. Tao, J. Zhang, Y. Xia, H. Huang, L. Y. Zhang, Y. P. Gan, C. Liang, W. K. Zhang, Sn^{4+} ion decorated highly conductive Ti_3C_2 MXene: promising lithium-ion anodes with enhanced volumetric capacity and cyclic performance, **ACS Nano** 10(2016) 2491-2499.

[22] L.Z. Sheng, S.C. Liang, T. Wei, J. Chang, Z.M. Jiang, L.H. Zhang, Q.H. Zhou, J.L. Zhou, L.L. Jiang, Z.J. Fan, Space-confinement of MnO nanosheets in densely stacked graphene: ultra-high volumetric capacity and rate performance for lithium-ion batteries, **Energy Storage Mater.** 12(2018) 94-102.

[23] X. Wang, L. Lv, Z. Cheng, J. Gao, L. Dong, C. Hu, L. Qu, High- density monolith of N- doped holey graphene for ultrahigh volumetric capacity of Li- ion batteries, **Adv. Energy Mater.** 6(2016) 1502100.

[24] J. Zhou, J. Qin, X. Zhang, C. S. Shi, E. Liu, J. J. Li, N. Q. Zhao, C. N. He, 2D space-confined synthesis of few-layer MoS_2 anchored on carbon nanosheet for lithium-ion battery anode, **ACS Nano** 9(2015) 3837-3848.

[25] J. J. He, C. J. Zhang, H. P. Du, S. L. Zhang, P. Hu, Z. H. Zhang, Y. L. Ma, C. S. Huang, G. L. Cui, Engineering vertical aligned MoS_2 on graphene sheet towards thin film lithium ion battery, **Electrochim. Acta.** 178(2015) 476-483.

[26] Z. Hu, Q. N. Liu, S. L. Chou, S. X. Dou, Advances and challenges in metal sulfides/selenides for next-generation rechargeable sodium-ion batteries, **Adv. Mater.** 29(2017) 1700606.

[27] Y. Liu, N. Zhang, H. Kang, M. Shang, L. Jiao, J. Chen, WS_2 nanowires as a high- performance anode for sodium- ion batteries, **Chem. Eur. J.** 21(2015) 11878-11884.

[28] C.B. Zhu, P. Kopold, W.H. Li, P. A. van Aken, J. Maier, Y. Yu, Engineering nanostructured electrode materials for high performance sodium ion batteries: a case study of a 3D porous interconnected WS_2/C nanocomposite, **J. Mater. Chem. A** 3(2015) 20487-20493.

[29] J. Billaud, F. Bouville, T. Magrini, C. Villevieille, A. R. Studart, Magnetically aligned graphite electrodes for high-rate performance Li-ion batteries, **Nat. Energy** 1(2016) 16097.

[30] J. Sander, R. Erb, L. Li, A. Gurijala, Y. M. Chiang, High-performance battery electrodes via magnetic templating, **Nat. Energy** 1(2016) 16099.

[31] Y. Xia, T. Mathis, M.-Q. Zhao, B. Anasori, A. Dang, Z. Zhou, H. Cho, Y. Gogotsi, S. Yang, Thickness-independent capacitance of vertically aligned liquid-crystalline Mxenes, **Nature** 557(2018) 409-412.

[32] Y. Xiao, S.H. Lee, Y.K. Sun, The application of metal sulfides in sodium ion batteries, **Adv. Energy Mater.** 7(2017) 1601329.

[33] H.M. Wang, Q. Yuan, D. Wang, G. Chen, X. Cheng, T. Kups, P. Schaaf, Disordered surface formation of WS_2 *via* hydrogen plasma with enhanced anode performances for lithium and sodium ion batteries, **Sustain. Energ. Fuels.** 3(2019) 865-874.

[34] X.Q. Xiong, W. Luo, X.L. Hu, C.J. Chen, L. Qie, D.F. Hou, Y.H. Huang, Flexible membranes of MoS_2/C nanofibers by electrospinning as binder-free anodes for high-performance sodium-ion batteries, **Sci. Rep.** 5(2015) 9254.

[35] X.L. Hu, W. Zhang, X.X. Liu, Y.N. Mei, Y.H. Huang, Nanostructured Mo-based electrode materials for electrochemical energy storage, **Chem. Soc. Rev.** 44(2015) 2376-2404.

[36] Y. Fang, Y. Y. Lv, F. Gong, A. A. Elzatahry, G. Zheng, D. Y. Zhao, Synthesis of 2D-mesoporous-carbon/MoS_2 heterostructures with well-defined interfaces for high-performance lithium-ion batteries, **Adv. Mater.** 28(2016) 9385-9390.

[37] S. Y. Chen, C. X. Zheng, M. S. Fuhrer, J. Yan, Helicity-resolved raman scattering of MoS_2, $MoSe_2$, WS_2, and WSe_2 atomic layers, **Nano Lett.** 15(4)(2015) 2526-2532.

[38] M. B. Sreedhara, Subhra Gope, B. Vishal, R. Datta, A.J. Bhattacharyya, C. N. Rao, Atomic layer deposition of crystalline epitaxial MoS_2 nanowall networks exhibiting superior performance in thin-film rechargeable Na-ion batteries, **J. Mater. Chem. A** 6(2018) 2302-2310.

[39] M. Nisula, M. Karppinen, Atomic/molecular layer deposition of lithium terephthalate thin films as high rate capability Li-ion battery anodes, **Nano Lett.** 16(2016) 1276-1281.

[40] X. Li, A. Lushington, Q. Sun, W. Xiao, J. Liu, B.Q. Wang, Y.F. Ye, K.Q. Nie, Y.F. Hu, Q.F. Xiao, R.Y. Li, J.H. Guo, T.K. Sham, X.L. Sun, Safe and durable high-temperature lithium-sulfur batteries *via* molecular layer deposited coating, **Nano Lett.** 16(2016) 3545-3549.

[41] S. Komaba, W. Murata, T. Ishikawa, N. Yabuuchi, T. Ozeki, T. Nakayama, A. Ogata, K. Gotoh, K. Fujiwara, Electrochemical Na insertion and solid electrolyte interphase for hard-carbon electrodes and application to Na-ion batteries, **Adv. Funct. Mater.** 21(**2011**) 3859-3867.

[42] C. Huang, J. Xiao, Y.Y. Shao, J.M. Zheng, W. D. Bennett, D.P. Lu, L. V. Saraf, M. Engelhard, L.W. Ji, J.G. Zhang, X.L. Li, G. L. Graff, J. Liu, Manipulating surface reactions in lithium-sulphur batteries using hybrid anode structures, **Nat. Commun.** 5(2014) 3015.

[43] D.W. Su, S.X. Dou, G.X. Wang, WS_2@graphene nanocomposites as anode materials for Na-ion batteries with enhanced electrochemical performances, **Chem. Commun.** 50(2014) 4192-4195.

[44] S. H. Choi, Y. C. Kang, Sodium ion storage properties of WS_2-decorated three-dimensional reduced graphene oxide microspheres, **Nanoscale** 7(2015) 3965-3970.

[45] Q.B. Guo, Y.F. Ma, T.T, Chen, Q.Y. Xia, M. Yang, H. Xia, Y. Yu, Cobalt sulfide quantum dot embedded N/S-doped carbon nanosheets with superior reversibility and rate capability for sodium-ion batteries, **ACS Nano** 11(2017) 12658-12667.

[46] Y.D. Zhang, P.Y. Zhu, L.L. Huang, J. Xie, S.C. Zhang, G.S. Cao, X.B. Zhao, Few- layered SnS_2 on few- layered reduced graphene oxide as na- ion battery anode with ultralong cycle life and superior rate capability, **Adv. Funct. Mater.** 25(2015) 481-489.

[47] J. Xu, J.J. Zhang, W.J. Zhang, C.S. Lee, Interlayer nanoarchitectonics of two- dimensional transition- metal dichalcogenides nanosheets for energy storage and conversion applications, **Adv. Energy Mater.** 7(2017) 1700571.

[48] E. M. Lotfabad, J. Ding, K. Cui, A. Kohandehghan, W. P. Kalisvaart, M. Hazelton, D. Mitlin, High-density sodium and lithium ion battery anodes from banana peels, **ACS Nano** 7(2014) 7115-7129.

[49] X.Q. Xie, M.Q. Zhao, B. Anasori, K. Maleski, C. E. Ren, J.W. Li, B.W. Byles, E. Pomerantseva, G.X. Wang, Y. Gogotsi, Porous heterostructured MXene/carbon nanotube composite paper with high volumetric capacity for sodium-based energy storage devices, **Nano Energy** 26(2016) 513-523.

[50] X. Hu, Y. Li, G. Zeng, J.C. Jia, H.B. Zhan, Z.H. Wen, Three-dimensional network architecture with hybrid nanocarbon composites supporting few-layer MoS_2 for lithium and sodium storage, **ACS Nano** 12(2018) 1592-1602.

[51] E.H. Wang, W. Xiang, R. Rajagopalan, Z.G. Wu, J.H. Yang, M.Z. Chen, B.H. Zhong, S.X. Dou, S.L. Chou, X.D. Guo, Y.M. Kang, Construction of 3D pomegranate-like Na3V2(PO4)3/conducting carbon composites for high-power sodium-ion batteries, **J. Mater. Chem. A** 6(2017) 9833-9841.

[52] K. Zhang, P. Li, M. Ma, J. H. Park, Core-shelled low-oxidation state oxides@reduced graphene oxides cubes *via* pressurized reduction for highly stable lithium ion storage, **Adv. Funct. Mater.** 26(2016) 2959-2965.

[53] Y.J. Liu, Z.X. Tai, T.F. Zhou, V. Sencadas, J. Zhang, L. Zhang, K. Konstantinov, Z.P. Guo, H.K. Liu, An all- integrated anode *via* interlinked chemical bonding between double- shelled–yolk-structured silicon and binder for lithium- ion batteries, **Adv. Mater.** 9(2017) 1703028.

[54] L. Yu, H.B. Wu, X.W. Lou, Self-templated formation of hollow structures for electrochemical energy applications, **Acc. Chem. Res.** 50(2)(2017) 293-301.

[55] C.J. Chen, Y. Zhang, Y.J. Li, Y.D. Kuang, J.W. Song, W. Luo, Y.B. Wang, Y.G. Yao, G. Pastel, J. Xie, L.P. Hu, Highly conductive, lightweight, low- tortuosity carbon frameworks as ultrathick 3D current collectors, **Adv. Energy Mater**. 7(2017) 1700595.

[56] C.J. Chen, S.M. Xu, Y.D. Kuang, W.T. Gan, J.W. Song, G.G. Chen, G. Pastel, B.Y. Liu, Y.J. Li, H. Huang, L.B. Hu, Nature- inspired tri- pathway design enabling high- performance flexible Li–O_2 batteries, **Adv. Energy Mater.** 9(2019) 1802964.

[57] L.S. Li, R.M. Erb, J.J. Wang, J. Wang, Y.M. Chiang, Fabrication of low- tortuosity ultrahigh-area- capacity battery electrodes through magnetic alignment of emulsion- based slurries, **Adv. Energy Mater.** 8(2018) 1802472.

[58] S.M. Xu, D.W. McOwen, L. Zhang, G.T. Hitz, C.W. Wang, Z.H. Ma, C.J. Chen, W. Luo, J.Q. Dai, Y.D. Kuang, E.M. Hitz, K. Fu, Y.H. Gong, E.D. Wachsman, L.B. Hu, All-in-one lithium-sulfur battery enabled by a porous-dense-porous garnet architecture, **Energy Storage Mater.** 15(2018) 458-464.

Conflict of Interest Form

- The authors declare no conflict of interest.

- All authors have participated in (a) conception and design, or analysis and interpretation of the data; (b) drafting the article or revising it critically for important intellectual content; and (c) approval of the final version.

- This manuscript has not been submitted to, nor is under review at, another journal or other publishing venue.

- The authors have no affiliation with any organization with a direct or indirect financial interest in the subject matter discussed in the manuscript.

Highlights

- An innovative physical sputtering method was used to construct WS_2 platelets film;
- The platelets anchored on the Al foil as additive-free thin anode for SIBs;
- The fabricated thin WS_2 anode had the superior volumetric capacity for SIBs;
- WS_2 film growth rate was up to 58 nm/min and the film is thickness-controllable.